Dalton Transactions

ROYAL SOCIETY OF CHEMISTRY

PAPER

View Article Online
View Journal | View Issue

Check for updates

Cite this: *Dalton Trans.*, 2025, **54**, 6653

Exploring pseudocapacitive performance in $Cr_2CT_x/NiFe_2O_4$ composites: experimental insights†

Madhushree R and Kalathiparambil Rajendra Pai Sunajadevi *

Received 22nd February 2025,
Accepted 16th March 2025

DOI: 10.1039/d5dt00446b

rsc.li/dalton

The growing demand for sustainable and efficient energy storage systems has driven the development of advanced, durable, and cost-effective materials. This study introduces heterostructures of 2D Cr_2CT_x MXene and $NiFe_2O_4$, leveraging their synergistic properties, such as high conductivity, surface termination groups (–OH, –O, and –F), tunable surface chemistry, and rich redox activity. Comprehensive structural and morphological characterization confirms the enhanced functionality of $Cr_2CT_x/NiFe_2O_4$, which exhibits a remarkable specific capacitance of 1719.5 F g^{-1} with 88% retention over 5000 cycles in a three-electrode system. Additionally, the asymmetric supercapacitor device demonstrates a specific capacitance of 486.66 F g^{-1}, an energy density of 97.66 W h kg^{-1}, and a power density of 1203.95 W kg^{-1}, retaining 94% of its capacitance after 5000 cycles. A plausible charge transfer mechanism in the composite is discussed, providing new insights into the synergistic $Cr_2CT_x/NiFe_2O_4$ heterostructures as high-performance materials for energy storage applications.

1. Introduction

The growing demand for sustainable and efficient energy storage technologies is reshaping the global energy landscape, aligning closely with the objectives of the Sustainable Development Goals (SDGs), particularly SDG 7, which emphasizes affordable and clean energy access. Addressing this need requires the development of advanced energy storage systems that integrate high efficiency, sustainability, and cost-effectiveness. A wide range of materials has been explored for energy storage applications, including conducting polymers, two-dimensional (2D) structures, transition metals, metal oxides/hydroxides, and carbon-based materials.[1] Among these, supercapacitors have gained significant attention for use in rechargeable batteries, fuel cells, and thermoelectric devices. Their unique advantages, such as rapid charge/discharge rates, long cycle life, high power density, and environmental compatibility, make them promising candidates for renewable energy systems, electric vehicles, and portable electronics.[2,3] Based on their charge storage mechanisms, supercapacitors are classified into three types: (i) electric double-layer capacitors (EDLCs), which store charge electrostatically at the electrode–electrolyte interface; (ii) pseudocapacitors, which rely on faradaic redox reactions; and (iii) hybrid supercapacitors, which integrate both EDLC and pseudocapacitive mechanisms. Pseudocapacitors, in particular, offer the advantage of higher energy density without compromising power density, with their performance largely dictated by the choice of electrode materials, which influence key parameters such as charge storage capacity, cycling stability, and overall efficiency.[4]

However, advancing beyond the above-mentioned materials is critical for meeting the growing energy demands and enhancing device performance. Recently, MXenes with a general formula $M_{n+1}X_nT_x$, where M stands for transition metals, X refers to boron, carbon and/or nitrogen, and T stands for terminating groups (–F, –Cl, –O, and –OH), have become the focus of extensive research and development with various applications.[5,6] Pristine MXenes often face challenges such as restacking tendencies and a lack of sufficient active sites, which can hinder ion accessibility and overall electrochemical performance. To overcome these challenges, several studies have explored modifying them to enhance their properties. For example, S. Mathew *et al.* reported the modification of a Ti_3C_2 MXene with CeO_2 (metal oxide) for improved supercapacitor performance.[7] Other works include MnO_2-N-heteroatom-modified Ti_3C_2 MXene[8] and Ti_3C_2 MXene composites with conducting polymers like PANI and PPy for supercapacitor applications.[9] Additionally, the $NiFe_2O_4/Ti_3C_2$ composite was investigated for hydrogen production by P. V. Shinde *et al.*,[10] and $Ti_3C_2/CoFe_2O_4/g\text{-}C_3N_4$ hybrids have been studied for their mul-

Department of Chemistry, Christ University, Bengaluru, 560029, India.
E-mail: sunajadevi.kr@christuniversity.in

† Electronic supplementary information (ESI) available. See DOI: https://doi.org/10.1039/d5dt00446b

tifunctional energy applications.[11] Ti-based MXenes, in general, have been extensively explored for various applications, including energy conversion and storage, environmental remediation, anticorrosion, and photocatalysis.[12] On the other hand, Cr-based composites remain relatively underexplored but show immense potential. For instance, a Cr_2CT_x MXene infused into a PVA polymer matrix was studied for hydrogen and oxygen evolution.[13] DFT studies by X. Zhang *et al.* demonstrated the modulation of oxygen electronic orbital occupancy in Cr-based MXenes for hydrogen evolution reactions.[14] Additionally, a $CoFe_2O_4$ modified Cr_2CT_x MXene was reported as a battery-type material with high specific capacitance and superior oxygen evolution reaction performance,[15] while $BiFeO_3$ nanoparticles were utilized as modifiers to enhance the supercapacitive properties of the Cr_2CT_x MXene.[16]

Cr-based MXenes and their modifications are still underexplored for electrochemical applications despite their unique advantages, including enhanced redox activity, highly tunable surface chemistry, and superior structural, mechanical, chemical, and thermal stability. These characteristics make Cr-based MXenes promising contenders within the MXene family, competing with more widely studied Ti-based MXenes that have been extensively explored for advanced energy storage systems. Cr_2CT_x is one such MXene, a member of the transition metal carbide family, which was synthesized from the hexagonal layered Cr_2AlC MAX phase (the $P6_3/mmc$ space group) by selectively etching away the aluminum layers.[17] The Cr_2CT_x MXene exhibits a unique structure characterized by strong covalent bonding between chromium and carbon atoms within its two-dimensional lattice. The removal of aluminum bonded to chromium within the crystal structure *via* metallic bonding creates a layered morphology with exposed terminal groups (–F, –O, and –OH) on the MXene surface, which not only enhances its hydrophilicity but also provides active sites for electrochemical reactions. These bonding interactions, combined with the high electrical conductivity of the MXene framework, make Cr_2CT_x an ideal candidate for applications in energy storage and conversion compared to graphene oxide (GO) and GO-based materials.[1]

Among potential candidates, spinel ferrites like $NiFe_2O_4$ offer unique advantages, including redox activity, high electrochemical stability, a high density of active sites, and high chemical stability, making them ideal candidates offering high pseudocapacitive performance. In the $Cr_2CT_x/NiFe_2O_4$ composite, the bonding interactions between the Cr_2CT_x MXene and $NiFe_2O_4$ are primarily driven by electrostatic and chemical forces, along with internal covalent bonding. The surface termination groups (–F, –O, –OH) on the Cr_2CT_x MXene play a crucial role in facilitating the interaction with $NiFe_2O_4$. These functional groups, particularly –OH and –O, can form hydrogen bonds or coordination bonds with metal ions in the $NiFe_2O_4$ structure (Ni–O/Fe–O), enhancing the stability and dispersion of the composite. The –F termination groups also help in tuning the electronic structure of the composite, improving the overall electrochemical performance. Impressive water splitting results motivated us to investigate supercapacitive performance.[17] Additionally, the strong ionic and covalent interactions between the MXene layers and the $NiFe_2O_4$ spheres and the synergistic properties contribute to a stable interface that supports efficient charge transfer and enhanced pseudocapacitive behavior. The synergy between $NiFe_2O_4$ and Cr_2CT_x leads to an improved overall electrochemical performance, making it an ideal choice for a composite.[10]

In this work, we explore new insights into the synthesis, properties, and pseudocapacitive behavior of a novel $Cr_2CT_x/NiFe_2O_4$ composite. The study focuses on the synthesis and detailed characterization of $Cr_2CT_x/NiFe_2O_4$, along with an in-depth investigation of its performance as an electrode material for pseudocapacitors using three-electrode and asymmetric supercapacitor devices. Furthermore, a comprehensive analysis is carried out to explore the synergistic influence of integrating $NiFe_2O_4$ with the Cr_2CT_x MXene on its pseudocapacitive performance. The selection of $NiFe_2O_4$ is based on its inherent redox activity, high specific capacitance, and ability to complement the conductivity and surface tunability of Cr_2CT_x. Thereby, this research offers a novel approach for designing high-performance, improved pseudocapacitance supercapacitor materials.

2. Experimental

2.1. Materials

Chromium metal powder (Cr) (>99.50% pure) was obtained from Kanton Laboratories, while graphite powder (C) (>99.50% pure) and aluminum metal powder (Al) (>99% pure) were purchased from Sisco Research Laboratories Pvt. Ltd. Nickel nitrate and ferric nitrate were obtained from Nice Chemicals Private Ltd. Ethanol, toluene, polyvinylidene fluoride (PVDF), *N*-methyl-2-pyrrolidone (NMP), and hydrofluoric acid (HF) were supplied by SD Fine Chemicals. All materials used were utilized without further purification.

2.2. Synthesis of $Cr_2CT_x/NiFe_2O_4$

The Cr_2AlC MAX phase was synthesized following our previous report.[18] Initially, chromium (Cr) and carbon (C) powders were mixed in a 2 : 1 weight ratio using a turbo mixer for 2 hours with toluene as a solvent. The mixture was then dried, pelletized, and heated in a tubular furnace at 1150 °C for 1 hour to form chromium carbide. The obtained material was then combined with aluminum (Al) powder in a 1 : 1.2 weight ratio, following the same mixing, drying, and pelletizing process. The pellets were again heated at 1150 °C for 1 h to obtain the Cr_2AlC MAX phase, which was subsequently crushed and sieved using a ~200 mesh for further studies. The Cr_2CT_x MXene was synthesized from the Cr_2AlC MAX phase through etching with HF for 45 min. The composite material, $Cr_2CT_x/NiFe_2O_4$, was prepared using a hydrothermal method. 1 mM nickel nitrate and 2 mM ferric nitrate were dissolved in 50 mL DI water under stirring for 60 min. Separately, an MXene solu-

tion was prepared by dispersing 100 mg of Cr_2CT_x in 10 mL of DI water, followed by sonication for 30 minutes. The solutions were then mixed, stirred, and transferred to an autoclave, where the reaction was carried out at 180 °C for 24 h. The resulting $Cr_2CT_x/NiFe_2O_4$ composite was thoroughly washed with DI water and ethanol and dried overnight at 60 °C. The synthesis strategy for $Cr_2CT_x/NiFe_2O_4$ is depicted in Fig. 1.

2.3. Materials characterization

Comprehensive characterization of the MXene composite, including structural, morphological, and elemental studies, was conducted using spectroscopic methods. The structural properties and crystallinity of the materials were investigated using a Rigaku Smart Lab X-ray diffractometer (XRD) with Cu-Kα radiation (λ = 0.154 nm). The functional groups were identified using a Shimadzu IR Spirit-L Fourier transform infrared spectrometer (FTIR). Thermal stability was evaluated using a PerkinElmer thermogravimetric analyzer (TGA). The specific surface area and pore size distribution of the material were determined using Brunauer–Emmett–Teller (BET) analysis based on nitrogen adsorption–desorption isotherms. The morphology and elemental composition were characterized using Apreo S LoVac field emission scanning electron microscopy (FESEM) coupled with energy-dispersive X-ray spectroscopy (EDS), along with transmission electron microscopy (TEM) on a JEOL-2100 Plus. The surface chemical composition and oxidation states of the material were analyzed using X-ray photoelectron spectroscopy (XPS) with a PHI Versaprobe III system.

2.4. Electrochemical measurements

Electrochemical analyses were performed on a CHI608E electrochemical workstation (CH Instruments Inc., USA) configured with a three-electrode system. For supercapacitance measurements, a calomel electrode served as the reference, a platinum wire was used as the counter electrode, and the working electrode was prepared by coating catalyst ink on a Ni foam substrate. The $Cr_2CT_x/NiFe_2O_4$ (0.5 g) active material was mixed with PVDF (0.0451 g) and activated carbon (0.144 g) in NMP (60 μL) to form a homogeneous suspension *via* sonication/grinding using a motor and pestle. The resulting mixture was then applied to Ni foam and dried overnight at 60 °C. The experiments were carried out using 3 M KOH as the electrolyte.

$$C_s = \frac{I\Delta t}{m\Delta V} \quad (1)$$

$$\text{Energy density} = \frac{C_s \times (\Delta V)^2}{2 \times 3.6} \quad (2)$$

$$\text{Power density} = \frac{3600 \times \text{energy density}}{\Delta t} \quad (3)$$

An aqueous slurry of the sample was drop-cast onto Ni foam to fabricate the working electrode. The slurry was prepared by mixing $Cr_2CT_x/NiFe_2O_4$ with activated carbon, PVDF, and 60 μL of NMP, followed by drying overnight. The supercapacitive performance of the prepared electrode was evaluated at room temperature using cyclic voltammetry (CV), galvanostatic charge–discharge (GCD), and electrochemical impedance spectroscopy (EIS). Key performance parameters, including specific capacitance (C_s), energy density, and power density, were calculated using eqn (1)–(3). This experimental approach facilitated a thorough investigation of the supercapacitive properties of the synthesized electrode material.

3. Results and discussion

3.1. Structural, thermal, morphological, and chemical characterization of $Cr_2CT_x/NiFe_2O_4$

The structural properties of the synthesized electrocatalysts, Cr_2CT_x MXene and the $Cr_2CT_x/NiFe_2O_4$ composite, were evaluated using X-ray diffraction (XRD) analysis. Fig. 2a (black trace) shows the XRD profile of the pristine Cr_2CT_x MXene, while the blue trace illustrates the XRD pattern of $Cr_2CT_x/NiFe_2O_4$, both analyzed in the 2θ range of 10–80°. For the Cr_2CT_x MXene, the diffraction peaks at 2θ values of 13.8° (002), 26.5° (004), 35.1° (100), 40.1° (101), 42.1° (103), 43.1° (104), 54.6° (106), 56.8° (107) and 77.1° (109) correspond to the (*hkl*) planes, as per JCPDS Card No. 29-0017, consistent with the previously reported literature.[19–21] XRD pattern of pristine $NiFe_2O_4$, provided in the supplementary file (Fig. S1†), matches well with

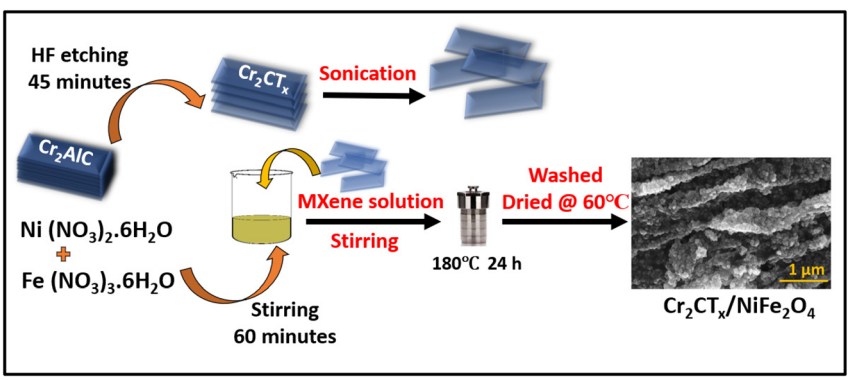

Fig. 1 Synthesis strategy for the $Cr_2CT_x/NiFe_2O_4$ composite.

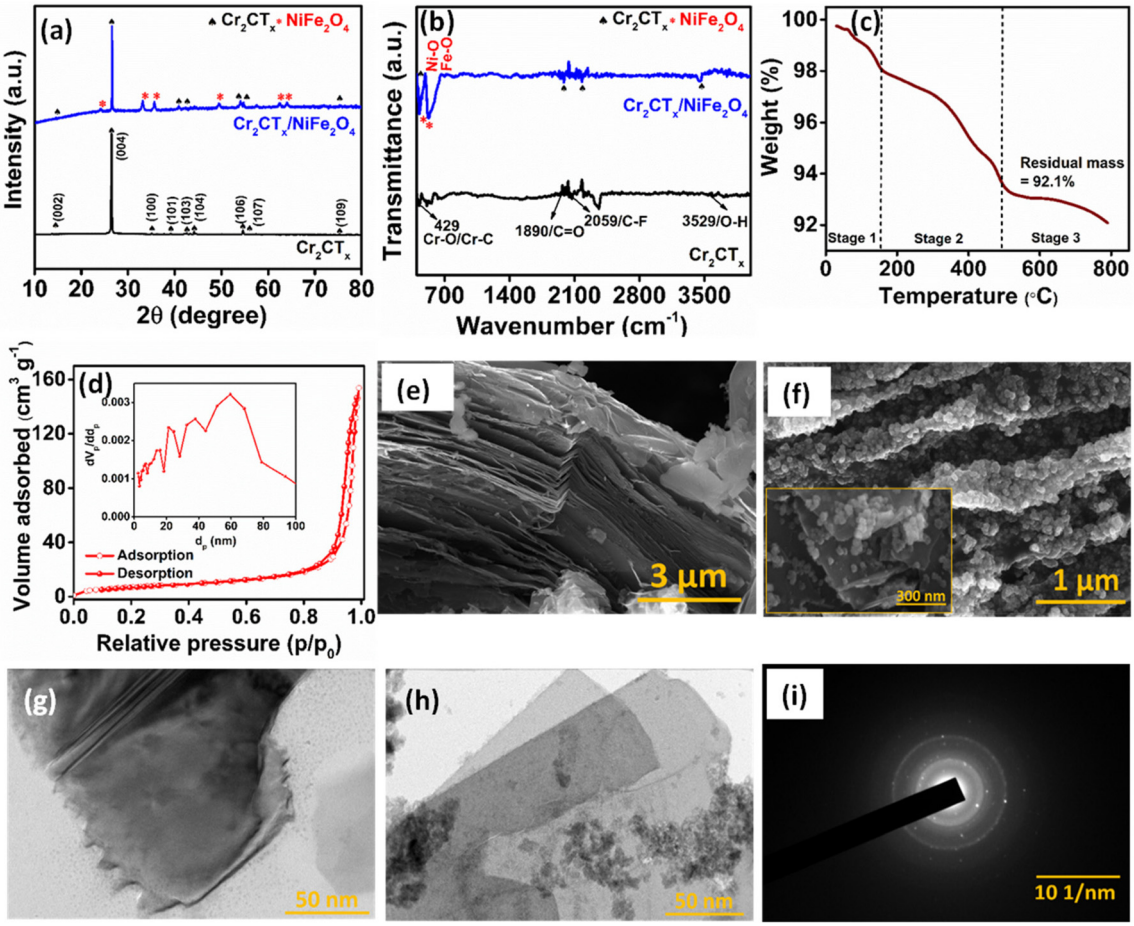

Fig. 2 Comparison between Cr_2CT_x and $Cr_2CT_x/NiFe_2O_4$ (a) XRD pattern and (b) FTIR spectra, (c) TGA profile, (d) BET isotherm with BJH for $Cr_2CT_x/NiFe_2O_4$, and FESEM images of (e) Cr_2CT_x and (f) $Cr_2CT_x/NiFe_2O_4$. TEM images of (g) Cr_2CT_x and (h) $Cr_2CT_x/NiFe_2O_4$ and (i) SAED pattern of $Cr_2CT_x/NiFe_2O_4$.

the JCPDS Card No. 10-0325, confirming the highly crystalline sharp peaks of the spinel phase. However, a few existing peaks indexed at 33.1°, 36.1°, 49.4°, and 64.1° exhibit enhanced intensity, which can be attributed to the presence of Fe in its amorphous Fe_3O_4 form.[22] In the $Cr_2CT_x/NiFe_2O_4$ composite (blue trace), the characteristic peaks of the Cr_2CT_x MXene are observed alongside the diffraction peaks of cubic $NiFe_2O_4$ spheres, aligning with JCPDS Card No. 10-0325.[23] Notably, the peaks of the Cr_2CT_x MXene are marked (♠), while the distinct twin doublets (33.2, 35.8°, and 62.3, 64.2°) and other peaks assigned for $NiFe_2O_4$ are marked (*) in the XRD pattern of the composite material. These peaks are slightly broader and less intense in $Cr_2CT_x/NiFe_2O_4$, indicating a change in crystallinity, while the presence of $NiFe_2O_4$ spheres between the MXene layers likely influences the interlayer spacing, as evidenced by the increased intensity of the (002) plane, highlighting the enhanced crystallinity of the composite material. These findings indicate the successful incorporation of the spinel structure within the MXene framework, consistent with prior studies,[24] and validate the formation of the composite through the observed structural modifications.

An FTIR analysis was conducted to identify the functional groups on the surface of the electrocatalysts. In Fig. 2b, the composite shows (blue trace) characteristic bands in the range of 450–650 cm^{-1} corresponding to Cr–O/Cr–C (429 cm^{-1}), Ni–O (626 cm^{-1}), and Fe–O (488 cm^{-1}) stretching vibrations, indicating the presence of both Cr_2CT_x and $NiFe_2O_4$.[25,26] The bands at 3450 cm^{-1} and 2059 cm^{-1} are attributed to the O–H stretching and C–F bond vibrations, respectively. The thermal stability of $Cr_2CT_x/NiFe_2O_4$ was assessed using thermogravimetric analysis (TGA) up to 800 °C at a heating rate of 10 °C min^{-1}. The composite demonstrated an impressive residual mass of 92.1%, with three stages of weight loss observed during the analysis (Fig. 2c). In the first stage (~180 °C), the mass loss is attributed to the desorption of adsorbed water molecules. The second stage (180–500 °C) is due to the loss of lattice water and the onset of oxidation accompanied by exothermic effects.[27] Furthermore, beyond 500 °C there is a gradual and constant decrease in mass, which was observed, and it continues until 800 °C. This minimal weight loss highlights its superior thermal stability.[28] Fig. 2d presents the nitrogen adsorption–desorption isotherm

of the $Cr_2CT_x/NiFe_2O_4$ composite. The analysis revealed a notable specific surface area of 27.04 $m^2\ g^{-1}$, characterized by an H3 hysteresis loop and a Type III adsorption isotherm. The pore diameter (d_p) ranged between 15 nm and 25–40 nm, indicating a mesoporous structure, while a macroporous feature with a d_p value of 59 nm was observed, as shown in the inset of Fig. 2d. These findings align well with the morphological insights obtained from the FESEM analysis discussed below.

Field emission scanning electron microscopy (FESEM) analysis was employed to examine the surface morphology of the synthesized electrocatalysts, as shown in Fig. 2e and f. The Cr_2CT_x MXene derived from the MAX phase exhibited a characteristic multi-layered, accordion-like structure (Fig. 2e). The $Cr_2CT_x/NiFe_2O_4$ composite displayed spherical $NiFe_2O_4$ nanoparticles distributed on and between the MXene layers (Fig. 2f). The presence of these nanospheres effectively mitigates the restacking of MXene sheets, enhancing the material's structural stability. The EDX analysis confirmed the elemental composition of the composite, revealing the following weight percentage: Cr (10.09%), O (25.42%), Ni (1.51%), C (13.38%) and Fe (48.55%), the increased wt% of Fe can be correlated with the XRD analysis discussed above and therefore, the Fe content observed in EDS analysis is dominated by the crystalline phase: a $NiFe_2O_4$ spinel structure. In contrast, a small fraction is in the amorphous Fe_3O_4 phase. TEM analysis provided further insights into the surface morphology. The TEM micrograph of Cr_2CT_x (Fig. 2g) shows a distinct sheet-like morphology. In the $Cr_2CT_x/NiFe_2O_4$ composite (Fig. 2h), spherical spinels are observed integrated within the MXene sheets. Additionally, the SAED pattern (Fig. 2i) confirms the crystalline nature of the material, consistent with the XRD results and previous studies.[20,29] This comprehensive morphological and structural analysis confirms the successful synthesis of the composite material.

X-ray photoelectron spectroscopy was performed to analyze the surface elements and valence states of the $Cr_2CT_x/NiFe_2O_4$ composite. The survey spectrum (Fig. 3a) confirms the presence of Cr, C, Ni, Fe, and O, validating the successful formation of the composite. The Cr 2p spectrum reveals two major peaks corresponding to Cr $2p_{3/2}$ and $2p_{1/2}$ (Fig. 3b). The peaks at binding energies of 574.5 eV, 576.6 eV, 579.1 eV, and 587.1 eV are attributed to Cr–C–Cr, Cr–C, and Cr–O, respectively.[30,31] In the C 1s spectra (Fig. 3c), the peaks at binding energies of 287, 286.2, and 284.9 eV, correspond to C═O, C–O/C–C, and C–Cr–T_x bonds, respectively.[32,33] The O 1s spectra (Fig. 3d) displayed peaks at 532.7, 531.5, and 531.1 eV, which can be attributed to metal bonded to the adsorbed water molecule, –OH groups and –O.[34,35] Fig. 3e depicts Ni 2p spectra, with $2p_{3/2}$ and $2p_{1/2}$ states with binding energies of 856.2eV and 873.8 eV, with two satellite peaks at 862.2 eV, and 880.2 eV, which are attributed to Ni–Fe and Ni–O bonding in the material with Ni^{2+}/Ni^{3+} oxidation states.[36] The Fe 2p illustrated in Fig. 3f indicates prominent peaks at 723.1 eV (Fe $2p_{1/2}$) and 709.7 eV (Fe $2p_{3/2}$), indicative of Fe^{3+} ions.[20,30]

3.2. Supercapacitance measurements

The Cr_2CT_x MXene demonstrates remarkable properties, including a layered architecture, exceptional electrical conductivity (due to its metallic nature, which enhances electron transfer), and a specific surface area, all of which are critical

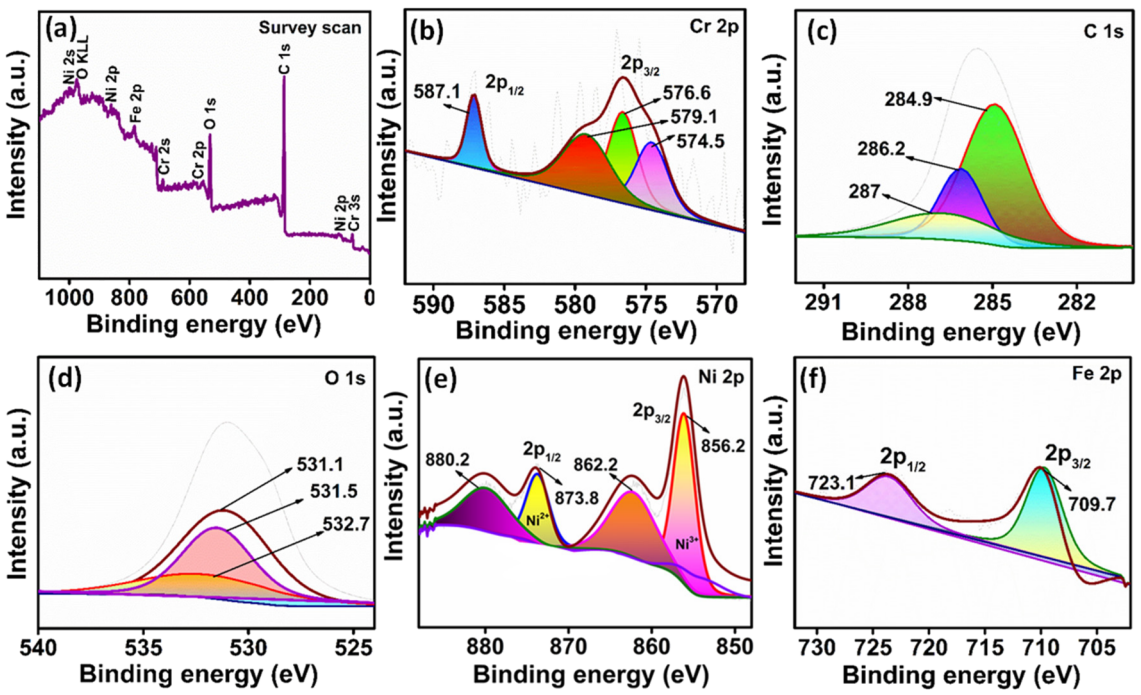

Fig. 3 (a) Survey scan of $Cr_2CT_x/NiFe_2O_4$ and deconvoluted XPS spectra of (b) Cr 2p, (c) C 1s, (d) O 1s, (e) Ni 2p and (f) Fe 2p.

for effective charge storage. The surface termination groups (–F, –O, –OH) play a vital role in enhancing pseudocapacitive behaviour by facilitating rapid and reversible redox reactions during electrochemical cycling. These groups also improve electrolyte wettability and promote ion transport at the electrode–electrolyte interface. The 2D structure of MXene allows efficient ion transport and electrolyte diffusion, reducing internal resistance and boosting energy storage capabilities. Moreover, the interlayer spacing of the Cr_2CT_x MXene can be tuned through modifications to optimize ion intercalation, further enhancing its capacitive properties. $NiFe_2O_4$, an inverse spinel, is recognized for its outstanding structural and

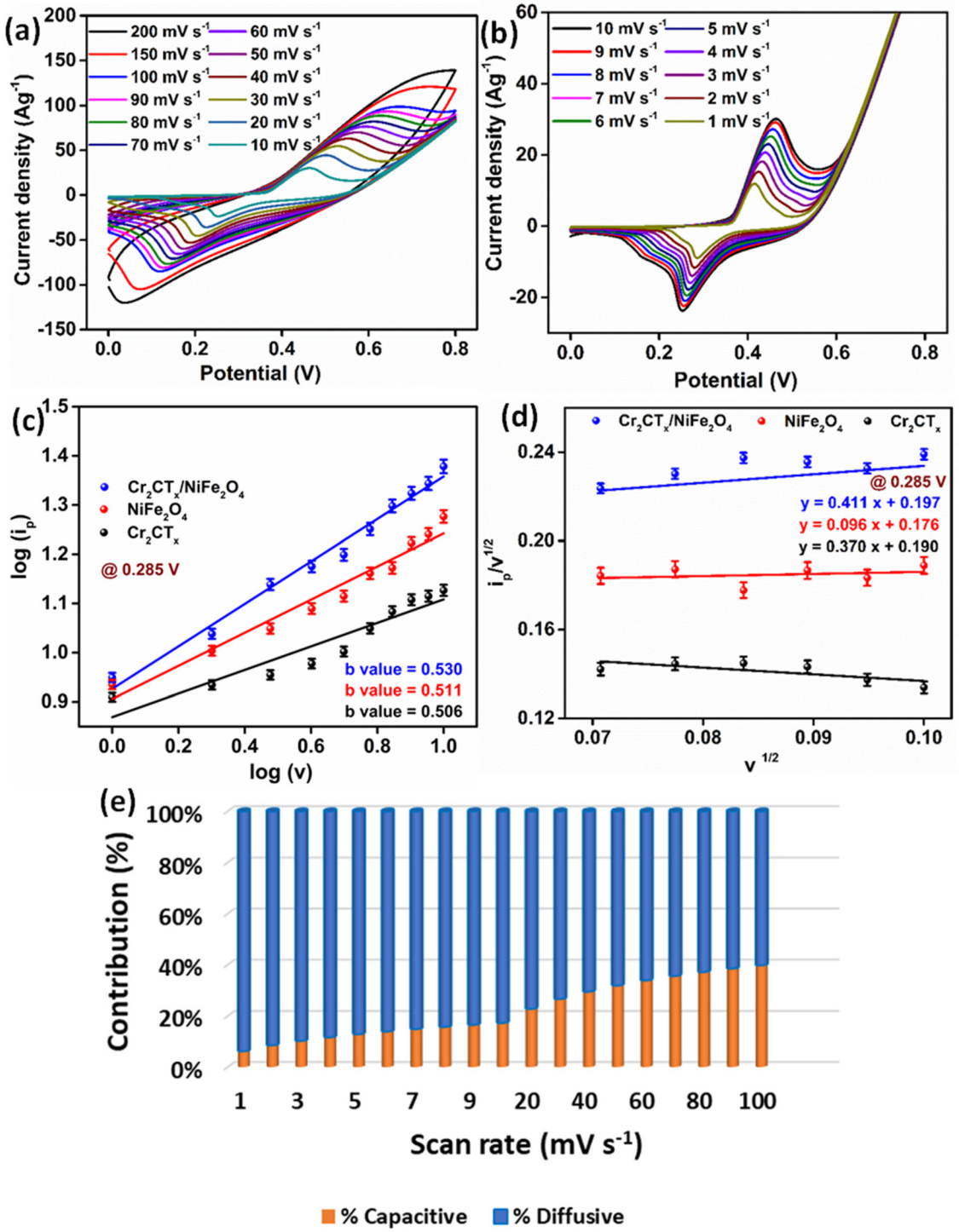

Fig. 4 Cyclic voltammograms at different scan rates: (a) high range from 200 to 10 mV s^{-1}, (b) low range from 10 to 1 mV s^{-1}, (c) linear plot of log(v) *vs.* log(i_p), (d) linear plot of $v^{\frac{1}{2}}$ *vs.* $i_p/v^{\frac{1}{2}}$, and (e) capacitive and diffusive contributions at different scan rates.

electrochemical characteristics, offering significant advantages over other spinels and state-of-the-art catalysts.[37,38] The mixed-valence Fe and Ni ions in their inverse spinel structure enable efficient electron transfer and robust redox activity, driving faradaic reactions effectively. Additionally, $NiFe_2O_4$ exhibits excellent chemical stability, electrical conductivity, and a large surface area, providing ample active sites for redox reactions and ensuring efficient energy storage with rapid charge–discharge cycles. When combined with the Cr_2CT_x MXene, $NiFe_2O_4$ synergistically enhances the composite's performance, resulting in a $Cr_2CT_x/NiFe_2O_4$ material that capitalizes on the strengths of both components. This also leads to superior capacitive performances by leveraging the robust electron transfer, enhanced ion transport, and abundant active sites provided by the composite structure.

The cyclic voltammogram (CV) profile of $Cr_2CT_x/NiFe_2O_4$ recorded at higher scan rates (200 to 10 mV s^{-1}) within the potential window of 0 to 0.8 V is shown in Fig. 4a. At a scan rate of 10 mV s^{-1}, two distinct peaks are observed at 0.284 V and 0.413 V, corresponding to reduction and oxidation processes, respectively, which deviate from the sharp triangular profiles typically seen in double-layer capacitance. These well-defined redox peaks confirm significant faradaic contributions, where $NiFe_2O_4$ enhances the electroactive sites and facilitates faradaic reactions. Furthermore, the intercalation and deintercalation of electrolyte ions within the layered structure of Cr_2CT_x validate the pseudocapacitive behavior of the material.[39] The CV profiles also demonstrate an increase in current density with increasing scan rates, leading to an expansion of the CV curve area. This behavior can be explained by the decrease in the diffusion layer thickness at higher scan rates, enhancing ion mobility. Consequently, the larger CV curve area at higher scan rates indicates improved specific capacity, underscoring the material's suitability for charge storage applications.

$$i_p = a(v)^b \quad (4)$$

$$i_p = k_1 v + k_2 (v)^{\frac{1}{2}} \quad (5)$$

To further analyze the charge storage dynamics, lower scan rate CV profiles (10–1 mV s^{-1}) were recorded (Fig. 4b) and analyzed using the Randles–Sevcik equation (eqn (4)) and power-law relationship (eqn (5)).[40] The *b*-value, determined from the $\log(i_p)$ *vs.* $\log(v)$ plot (Fig. 4c) at 0.285 V, was found to be 0.530 for $Cr_2CT_x/NiFe_2O_4$, 0.510 for $NiFe_2O_4$, and 0.506 for Cr_2CT_x. These values confirm that the charge storage is predominantly diffusion-controlled pseudocapacitance.[41]

To further substantiate these findings, eqn (5), where i_p refers to the peak current at a particular potential (here, we chose the potential to be 0.285 V, where the maximum current response was detected), and v is the scan rate in V s^{-1}. The surface capacitive ($k_1 v$) and diffusive contributions ($k_2 v^{\frac{1}{2}}$) were determined by plotting $\frac{i_p}{v^{1/2}}$ and $v^{1/2}$ (Fig. 4d). $Cr_2CT_x/NiFe_2O_4$, the slope (k_1) and *y*-intercept (k_2) were determined to be 0.411 and 0.197, respectively. These values were used to quantify the capacitive and diffusive contributions at different scan rates, as shown in Fig. 4e. At a scan rate of 1 mV s^{-1}, the diffusive and capacitive contributions for $Cr_2CT_x/NiFe_2O_4$ were calculated to be 93.81% and 6.18%, respectively, confirming a predominantly diffusion-controlled mechanism. However, as the scan rate increases from 1 to 100 mV s^{-1}, diffusion current contributions decrease from 60.25% to 93.81%, as ions have less time to diffuse fully at higher scan rates, while at lower scan rates, conducting ions have sufficient time to diffuse to and from the electrode surface, thereby significantly influencing the overall charge storage dynamics. Similar trends were observed for the pristine materials, where the diffusion-controlled contributions for $NiFe_2O_4$ decreased from 98.31% to 85.38%, and for Cr_2CT_x decreased from 94.19% to 61.87% over the same scan rate range. The synergistic behavior of the composite, combining the layered conductivity of Cr_2CT_x and the redox-active nature of $NiFe_2O_4$, enhances pseudocapacitive performance through efficient ion intercalation, faradaic reactions, and increased electroactive sites (Fig. 5). This confirms that $Cr_2CT_x/NiFe_2O_4$ is a highly effective electrode material for intercalation pseudocapacitors, with superior energy storage capabilities driven by diffusion-controlled charge storage mechanisms and optimized interfacial dynamics.

Fig. 6a compares the CV profiles of $Cr_2CT_x/NiFe_2O_4$ (blue trace), $NiFe_2O_4$ (red trace), Cr_2CT_x (black trace), and bare Ni foam (green trace) at a scan rate of 10 mV s^{-1}, recorded within a potential window from 0 to 0.8 V. The CV profile of bare Ni foam exhibits negligible contribution as compared to the composite's redox peaks. This confirms that the dominant redox activity originates from the $Cr_2CT_x/NiFe_2O_4$ composite. These peaks correspond to the reversible redox transitions of Ni^{2+}/Ni^{3+} and Fe^{2+}/Fe^{3+}, facilitating charge storage through faradaic processes. Furthermore, these redox peaks in the composite arise from the synergistic interaction between the Cr_2CT_x

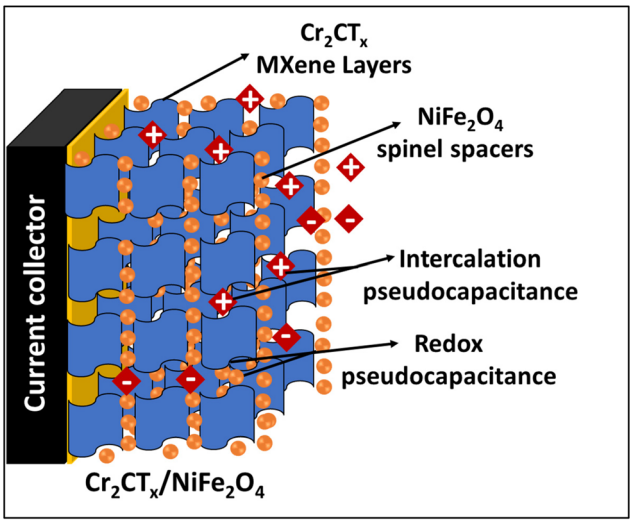

Fig. 5 A possible illustration of the intercalation and redox pseudocapacitive mechanisms in $Cr_2CT_x/NiFe_2O_4$.

MXene and $NiFe_2O_4$. The area under the CV curves, which directly correlates with the charge storing capacity of the electrode material, shows that $Cr_2CT_x/NiFe_2O_4$ exhibits a significantly larger CV area compared to pristine materials. This indicates superior charge storage per unit mass, translating into higher specific capacitance and enhanced electrochemical performance. The improved performance can be attributed to the synergistic interaction between the MXene and the spinel structure.

The galvanostatic charge–discharge (GCD) profiles presented in Fig. 6b further highlight the charge storage capabilities of the materials. The GCD curves for $Cr_2CT_x/NiFe_2O_4$ (blue trace), $NiFe_2O_4$ (red trace), and Cr_2CT_x (black trace) were recorded at a current density of 1 A g^{-1} within a potential

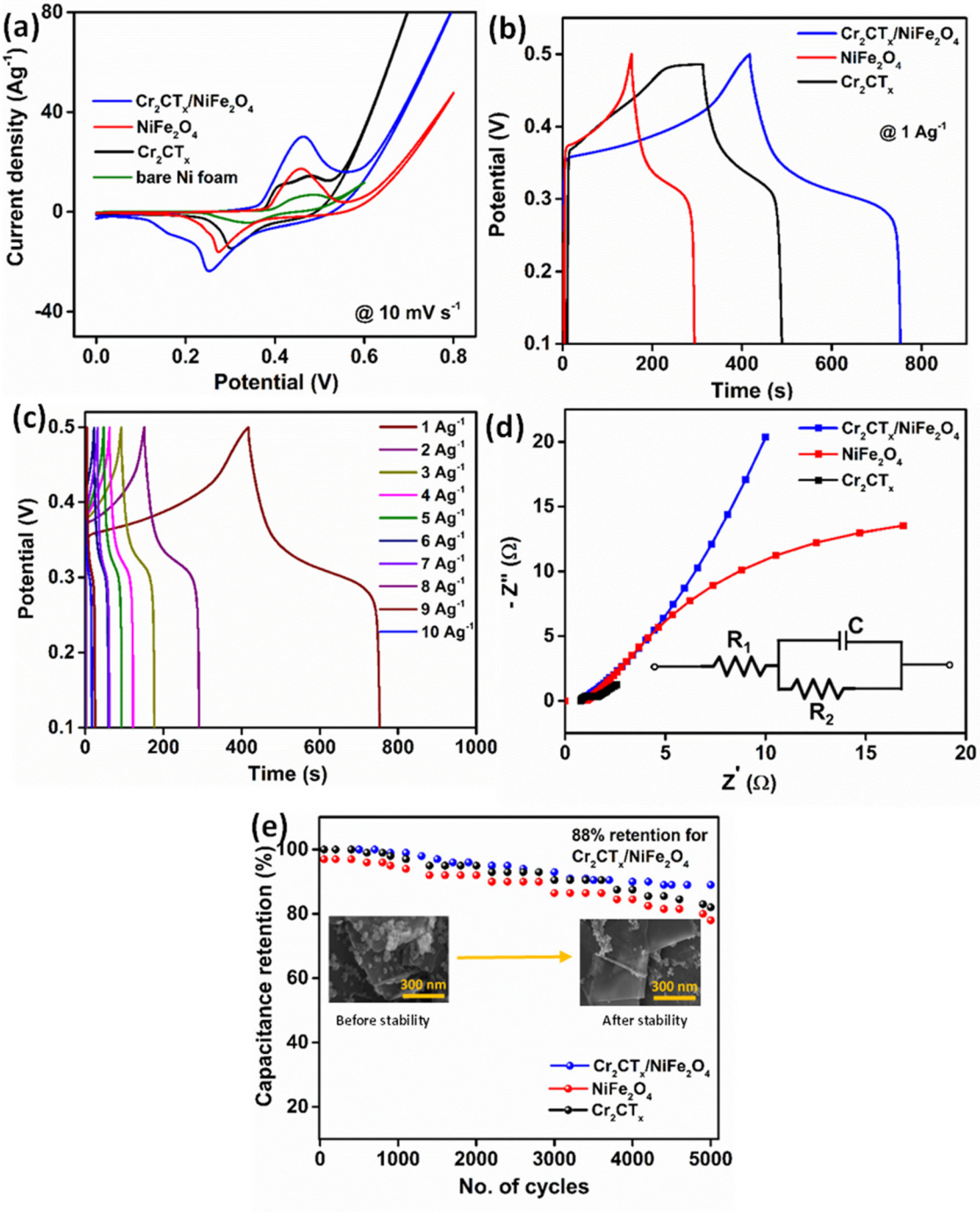

Fig. 6 (a) Comparison of the CV profile of $Cr_2CT_x/NiFe_2O_4$, Cr_2CT_x and $NiFe_2O_4$ at 10 mV s^{-1}, (b) GCD curves of $Cr_2CT_x/NiFe_2O_4$ and comparison plots of $Cr_2CT_x/NiFe_2O_4$, Cr_2CT_x and $NiFe_2O_4$, (c) GCD curves at 1 A g^{-1}, (d) Nyquist plot, and (e) stability test (inset: comparison of SEM images before and after cycling) using a three-electrode setup.

window of 0.1–0.5 V. The distinctive pseudocapacitive characteristics of the composite material are evident from the shape of its GCD curve. Among the materials, $Cr_2CT_x/NiFe_2O_4$ achieved the highest specific capacitance, C_s (calculated using eqn (1)) value of 1719.5 F g^{-1}, compared to 690.5 F g^{-1} for $NiFe_2O_4$ and 921 F g^{-1} for Cr_2CT_x. The energy density of the materials, calculated using eqn (2), was determined to be 38.21 W h kg^{-1}, 15.90 W h kg^{-1}, and 21.23 W h kg^{-1} for $Cr_2CT_x/NiFe_2O_4$, $NiFe_2O_4$, and Cr_2CT_x, respectively. While the power density, calculated using eqn (3), was 400 W kg^{-1} for $Cr_2CT_x/NiFe_2O_4$ and 414.78 W kg^{-1} for $NiFe_2O_4$, and 436.71 W kg^{-1} for Cr_2CT_x. Fig. 6c demonstrates the GCD profile of $Cr_2CT_x/NiFe_2O_4$ recorded at various current densities ranging from 1 to 10 A g^{-1}. The enhanced charge–discharge performance is primarily due to the redox-active capacity $NiFe_2O_4$ spheres, which reduces MXene layer stacking, improves interlayer spacing, provides redox active sites, and facilitates faster ion transport kinetics. Electrochemical impedance spectroscopy (EIS) data (Fig. 6d) further substantiate these findings. The Nyquist plot and Randles equivalent circuit reveal the charge transfer resistance R_{ct}, representing the resistance associated with charge transfer across the electrode–electrolyte interface. The $Cr_2CT_x/NiFe_2O_4$ (blue trace) demonstrated the lowest R_{ct} value of 1.12 Ω, aligning with its highest specific capacitance. In comparison, the R_{ct} values for $NiFe_2O_4$ (red trace) and Cr_2CT_x (black trace) were 1.52 Ω and 1.67 Ω, respectively. The stability tests over 5000 charge–discharge cycles at a current density of 20 A g^{-1} (Fig. 6e) revealed capacitance retention of 88%, 80%, and 83% for $Cr_2CT_x/NiFe_2O_4$, $NiFe_2O_4$, and Cr_2CT_x, respectively. Post-cycling SEM analysis for $Cr_2CT_x/NiFe_2O_4$@Ni foam shows intact MXene layers with spherical $NiFe_2O_4$ nanoparticles. This morphology shows no significant structural disruptions even after 5000 cycles (inset: Fig. 6e). This observation aligns with the high capacitance retention, reinforcing the material's stability and potential for long-term energy storage applications.

Additionally, the existing literature on the supercapacitor performance of MXenes modified with spinel-like structures is reviewed and discussed. I. Ayman *et al.* synthesized $CoFe_2O_4/Ti_3C_2T_x$ using HF etching and sonication, and examined its capacitive behavior in 1 M KOH, achieving a specific capacitance of 1268 F g^{-1} at 1 A g^{-1}.[42] The $MnCo_2O_4$@MXene demonstrated a specific capacitance of 806.67 F g^{-1} in a three-electrode setup and 20.94 F g^{-1} at 1 A g^{-1} in an asymmetric device.[43] The $CoFe_2O_4/Cr_2CT_x$ composite, studied in 3M KOH, displayed impressive capacitances of 1909 F g^{-1} and 459 F g^{-1} at 1 A g^{-1}, with the asymmetric device showing a slightly lower C_s value.[15] N.A. Althubiti *et al.* investigated the role of nickel foam in the $MnFe_2O_4$/MXene/NF composite for supercapacitor applications, achieving a capacitance of 1268.75 F g^{-1} at 1 A g^{-1}.[44] T. Yaqoob *et al.* reported the $Ti_3C_2T_x/Ag_2CrO_4$ composite, synthesized *via* etching and coprecipitation, revealing a significant variation in specific capacitance in acidic and basic electrolytes.[45] In 0.1 M H_2SO_4, the specific capacitance was 525 F g^{-1} at 10 mV s^{-1}, while in 1 M KOH, it was 75 F g^{-1} at 20 mV s^{-1}.[45] Lastly, MXene/$CoFe_2O_4$/g-C_3N_4, a ternary composite in 3 M KOH, achieved a specific capacitance of 1506 F g^{-1} at 5 A g^{-1}.[11] These studies highlight the diverse methodologies and electrolyte choices used in fabricating MXene-based composites with promising energy storage performances. Furthermore, as reports on the Cr_2CT_x MXene for supercapacitors are limited, we have included a comparison chart with available studies on Cr_2CT_x as well as other MXene family materials modified with spinel like materials in Table 1.

3.2.1 Fabrication of an asymmetric supercapacitor device. An asymmetric supercapacitor device was fabricated using the $Cr_2CT_x/NiFe_2O_4$ MXene composite as the current collector and activated carbon as the counter electrode, with 3 M KOH as the electrolyte. The CV profiles, shown in Fig. 7a, were recorded within a potential range of 0–1.4 V at scan rates ranging from 10 mV s^{-1} to 100 mV s^{-1}. At lower scan rates, the CV curves exhibited a quasi-rectangular shape, indicating electric double layer capacitance (EDLC) behavior primarily contributed by activated carbon in a two-electrode configuration. The presence of subtle redox peaks further signifies the pseudocapacitive contribution from the $Cr_2CT_x/NiFe_2O_4$ composite, likely arising from the redox activity of $NiFe_2O_4$ and the surface terminations of Cr_2CT_x. The symmetry of the CV curves around the zero-current axis demonstrates efficient charge–discharge behavior. The GCD profiles (Fig. 7b) display a nearly triangular shape with slight non-linearity, characteristic of the synergistic EDLC and pseudocapacitive behavior of the electrode material. The $Cr_2CT_x/NiFe_2O_4$ composite achieved a high specific capacitance of 486.66 F g^{-1} at a

Table 1 Comparison of synthesis strategies and specific capacitance with the reported literature on supercapacitors

Sl no.	Electroactive material	Synthesis strategy	Electrolyte	Specific capacitance (C_s) in F g^{-1}/ current density	Asymmetric device specific capacitance (C_s) in F g^{-1}	Ref.
1	$CoFe_2O_4/Ti_3C_2T_x$	HF etching, sonication	1 M KOH	1268@1 A g^{-1}	—	42
2	$MnCo_2O_4$@MXene	HF etching, hydrothermal	1 M KOH	807@1 A g^{-1}	20.9@1 A g^{-1}	43
3	$CoFe_2O_4/Cr_2CT_x$	HF etching, ultra-sonication	3 M KOH	1909@1 A g^{-1}	459@1 A g^{-1}	15
4	$MnFe_2O_4$/MXene/NF	HF etching, ultra-sonication	2 M KOH	1269@1 A g^{-1}	—	44
5	$Ti_3C_2T_x/Ag_2CrO_4$	HF etching, co-precipitation	0.1 M H_2SO_4, 1 M KOH	525@10 mV s^{-1}, 75@20 mV s^{-1}	—	45
6	MXene/$CoFe_2O_4$/g-C_3N_4	HF etching, ultra-sonication	3 M KOH	1506@5A g^{-1}	340.2@2 A g^{-1}	11
7	$Cr_2CT_x/NiFe_2O_4$	HF etching, hydrothermal	3 M KOH	1719@1A g^{-1}	486.6@1 A g^{-1}	**This work**

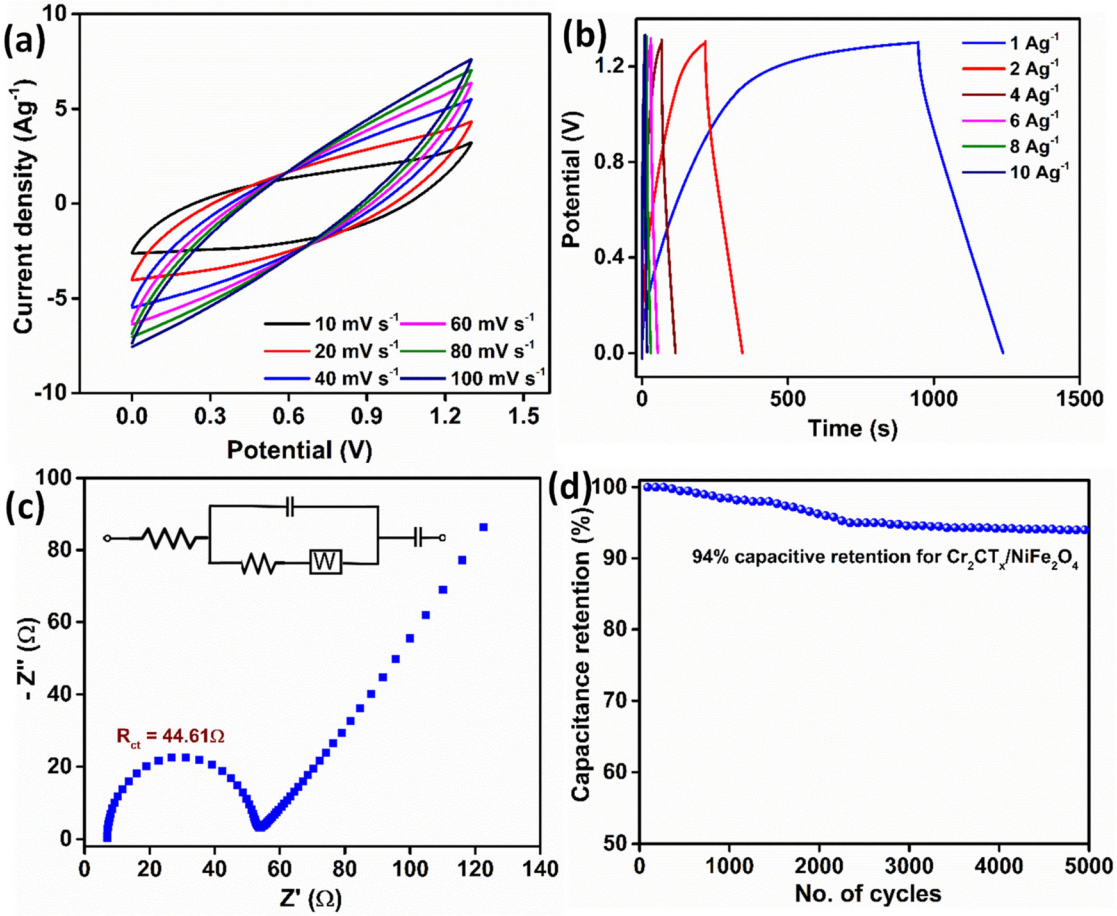

Fig. 7 (a) CV profile, (b) GCD curve, (c) Nyquist plot and (d) stability test of $Cr_2CT_x/NiFe_2O_4$ using a two-electrode setup.

current density of 1 A g^{-1} in a two-electrode configuration. The device delivered an impressive energy density of 97.66 W h kg^{-1}, along with a power density of 1203.95 W kg^{-1}, highlighting its suitability for high-performance energy storage applications.

The Nyquist plot, fitted with a Randles equivalent circuit (Fig. 7c), demonstrated a charge transfer resistance of 44.61 Ω, indicating excellent conductivity and efficient charge transfer at the electrode–electrolyte interface. The nearly vertical line in the low-frequency region suggests superior capacitive behavior and ion diffusion in the asymmetric device. Additionally, the cycling stability test (Fig. 7d) revealed that the device retained 94% of its initial capacitance after 5000 charge–discharge cycles at a constant current density, highlighting its robust durability and stability over extended cycles.

4. Conclusion

In conclusion, a novel $Cr_2CT_x/NiFe_2O_4$ electroactive composite was successfully synthesized *via* a simple hydrothermal process by integrating the Cr_2CT_x MXene with the $NiFe_2O_4$ spinel. Extensive structural, thermal, morphological, and chemical characterization for $Cr_2CT_x/NiFe_2O_4$ was conducted. XRD analysis verified the composite's synthesis, while FESEM imaging revealed the morphology, with $NiFe_2O_4$ spheres intercalated within the well-dispersed multi-layered Cr_2CT_x MXene. The $NiFe_2O_4$ spheres contributed to redox activity by enhancing active sites, while Cr_2CT_x provided excellent electrical conductivity, along with enhanced structural, chemical, and morphological stability, promoting improved charge storage. The composite exhibited remarkable pseudocapacitive performance, achieving a remarkable specific capacitance of 1719.5 F g^{-1} with 88% retention after 5000 cycles in a three-electrode system. Furthermore, the asymmetric supercapacitor device demonstrates a specific capacitance of 486.66 F g^{-1}, an energy density of 97.66 W h kg^{-1}, and a power density of 1203.95 W kg^{-1}, retaining 94% of its capacitance over 5000 cycles with exceptional cycling stability, thus showing great promise as a candidate for next-generation supercapacitors.

Author contributions

Madhushree R.: conceptualization, investigation, data curation, methodology, formal analysis, and writing the original

draft. Kalathiparambil Rajendra Pai Sunajadevi: conceptualization, supervision, formal analysis, validation, and writing – review and editing.

Data availability

The data that support the findings of this study are available from the corresponding author, [Kalathiparambil Rajendra Pai Sunajadevi, sunajadevi.kr@christuniversity.in], upon reasonable request. Due to confidentiality agreements and ethical considerations, the data are not publicly available.

Conflicts of interest

The authors declare that they have no known competing financial interests or personal relationships that could have appeared to influence the work reported in this paper.

Acknowledgements

The authors express their gratitude to CIF, Christ University, Bangalore, and the Department of Materials Engineering, Indian Institute of Science (IISc), Bangalore, for the instrumentation and characterization facility. Madhushree R acknowledges the Government of Karnataka, Backward Classes Welfare Department, for the PhD scholarship (2022PHD7645232).

References

1 M. Pandey, K. Deshmukh, A. Raman, A. Asok, S. Appukuttan and G. R. Suman, *Renewable Sustainable Energy Rev.*, 2024, **189**, 114030.
2 X. Hong, J. He, C. Duan, G. Wang and B. Liang, *Renewable Sustainable Energy Rev.*, 2025, **209**, 115134.
3 L. Li, F. Wang, J. Zhu and W. Wu, *Dalton Trans.*, 2017, **46**, 14880–14887.
4 S. Banerjee, B. Mordina, P. Sinha and K. K. Kar, *J. Energy Storage*, 2025, **108**, 115075.
5 S. Gokul Eswaran, M. Rashad, A. Santhana Krishna Kumar and A. F. M. El-Mahdy, *Chem. – Asian J.*, 2025, **20**, 4.
6 M. Y. Bhat, W. A. Adeosun, K. Prenger, Y. A. Samad, K. Liao, M. Naguib, S. Mao and A. Qurashi, *Adv. Compos. Hybrid Mater.*, 2025, **8**, 52.
7 S. Mathew and K. R. Sunaja Devi, *Colloids Surf., A*, 2024, **684**, 133170.
8 S. Mathew and K. R. Sunaja Devi, *Int. J. Hydrogen Energy*, 2024, **71**, 1283–1292.
9 S. M. Varghese, V. V. Mohan, S. Suresh, E. Bhoje Gowd and R. B. Rakhi, *J. Alloys Compd.*, 2024, **973**, 172923.
10 P. V. Shinde, P. Mane, B. Chakraborty and C. Sekhar Rout, *J. Colloid Interface Sci.*, 2021, **602**, 232–241.
11 S. Mathew, K. R. Sunaja Devi, B. Saravanakumar and D. Pinheiro, *J. Alloys Compd.*, 2024, **1008**, 176488.
12 M. Yadav, M. Kumar and A. Sharma, *ACS Appl. Nano Mater.*, 2024, **7**, 9847–9867.
13 R. Madhushree, K. P. Chaithra, K. R. Sunaja Devi and T. P. Vinod, *New J. Chem.*, 2024, **48**, 17159–17166.
14 X. Zhang, L. Chen, Q. Sun, Y. Pang, X. Yang and Z. Yang, *Int. J. Hydrogen Energy*, 2021, **46**, 25457–25467.
15 B. S. Reghunath, K. R. Sunaja Devi, S. Rajasekaran, B. Saravanakumar, J. J. William and D. Pinheiro, *J. Energy Storage*, 2024, **84**, 110775.
16 B. S. Reghunath, K. R. Sunaja Devi, S. Rajasekaran, B. Saravanakumar, J. J. William and D. Pinheiro, *Electrochim. Acta*, 2023, **461**, 142685.
17 R. Madhushree and K. R. Sunaja Devi, *Surf. Interfaces*, 2024, **52**, 104849.
18 M. Ramachandra and S. D. Kalathiparambil Rajendra Pai, *Emergent Mater.*, 2024, DOI: **10.1007/s42247-024-00815-w**.
19 M. Shahbaz, N. Sabir, N. Amin, Z. Zulfiqar and M. Zahid, *Front. Chem.*, 2024, **12**, 1413253.
20 B. S. Reghunath, K. R. Sunaja Devi, S. Rajasekaran, B. Saravanakumar, J. J. William and D. Pinheiro, *Electrochim. Acta*, 2023, **461**, 142685.
21 Y. Li, G. Zhao, Y. Qian, J. Xu and M. Li, *J. Mater. Sci. Technol.*, 2018, **34**, 466–471.
22 V. A. J. Silva, P. L. Andrade, M. P. C. Silva, A. Bustamante, D. L. De Los Santos Valladares and J. Albino Aguiar, *J. Magn. Magn. Mater.*, 2013, **343**, 138–143.
23 T. M. Naidu and P. V. L. Narayana, *J. Nanosci. Technol.*, 2019, **5**, 769–772.
24 B. Shalini Reghunath, S. Rajasekaran, K. R. Sunaja Devi, B. Saravanakumar, J. J. William, D. Pinheiro, D. Govindarajan and S. Kheawhom, *J. Phys. Chem. Solids*, 2022, **171**, 110985.
25 T. S. Munonde, H. Zheng, M. S. Matseke, P. N. Nomngongo, Y. Wang and P. Tsiakaras, *Renewable Energy*, 2020, **154**, 704–714.
26 M. Alimohamadi, A. Khataee, S. Arefi-Oskoui, B. Vahid, Y. Orooji and Y. Yoon, *Ultrason. Sonochem.*, 2023, **93**, 106294.
27 Y. Wei, S. Zhang, D. Zhai and F. Kang, *Battery Energy*, 2023, **2**, 20220027.
28 E. P. Simonenko, I. A. Nagornov, A. S. Mokrushin, A. A. Averin, Y. M. Gorban, T. L. Simonenko, N. P. Simonenko and N. T. Kuznetsov, *Micromachines*, 2023, **14**, 725.
29 X. Zou, H. Liu, H. Xu, X. Wu, X. Han, J. Kang and K. M. Reddy, *Mater. Today Energy*, 2021, **20**, 100668.
30 S. Y. Pang, Y. T. Wong, S. Yuan, Y. Liu, M. K. Tsang, Z. Yang, H. Huang, W. T. Wong and J. Hao, *J. Am. Chem. Soc.*, 2019, **141**, 9610–9616.
31 B. Shalini Reghunath, D. Davis and K. R. Sunaja Devi, *Chemosphere*, 2021, **283**, 131281.
32 B. Soundiraraju, R. Raghavan and B. K. George, *ACS Appl. Nano Mater.*, 2020, **3**, 11007–11016.
33 S. A. Shah, T. Habib, H. Gao, P. Gao, W. Sun, M. J. Green and M. Radovic, *Chem. Commun.*, 2017, **53**, 400–403.

34 D. Lim, H. Kong, N. Kim, C. Lim, W. S. Ahn and S. H. Baeck, *ChemNanoMat*, 2019, **5**, 1296–1302.
35 S. S. Sangu, N. M. Illias, C. C. Ong, S. C. B. Gopinath and M. S. M. Saheed, *Bionanoscience*, 2021, **11**, 314–323.
36 Y. Wei, T. Li, H. Cong, X. Chen, S. Zhou, S. Han and J. Jiang, *J. Colloid Interface Sci.*, 2023, **651**, 1054–1069.
37 Y. Zhang, Y. Zhang, C. Li, X. Yan, S. Hu, R. Yin, Y. Wei, K. Gao and H. Gao, *Coord. Chem. Rev.*, 2024, **519**, 216103.
38 Z. Feng, P. Wang, Y. Cheng, Y. Mo, X. Luo, P. Liu, R. Guo and X. Liu, *J. Electroanal. Chem.*, 2023, **946**, 117703.
39 D. Gandla, F. Zhang and D. Q. Tan, *ACS Omega*, 2022, **7**, 7190–7198.
40 H. Shao, Z. Lin, K. Xu, P.-L. Taberna and P. Simon, *Energy Storage Mater.*, 2019, **18**, 456–461.
41 Y. Ge, X. Xie, J. Roscher, R. Holze and Q. Qu, *J. Solid State Electrochem.*, 2020, **24**, 3215–3230.
42 I. Ayman, A. Rasheed, S. Ajmal, A. Rehman, A. Ali, I. Shakir and M. F. Warsi, *Energy Fuels*, 2020, **34**, 7622–7630.
43 Q. Xia, W. Cao, F. Xu, Y. Liu, W. Zhao, N. Chen and G. Du, *J. Energy Storage*, 2022, **47**, 103906.
44 N. A. Althubiti, S. Aman and T. A. M. Taha, *Ceram. Int.*, 2023, **49**, 27496–27505.
45 T. Yaqoob, M. Rani, A. Mahmood, R. Shafique, S. Khan, N. K. Janjua, A. A. Shah, A. Ahmad and A. A. Al-Kahtani, *Materials*, 2021, **14**(20), 6008.